Article

Sr Doping and Oxygen Vacancy Formation in $La_{1-x}Sr_xScO_{3-\delta}$ Solid Solutions: Computational Modelling

Yuri A. Mastrikov [1,*] **Denis Gryaznov** [1] **Guntars Zvejnieks** [1] **Maksim N. Sokolov** [1] **Māra Putniņa** [1] **and Eugene A. Kotomin** [1,2]

1   Institute of Solid State Physics, University of Latvia, Kengaraga 8, LV-1063 Riga, Latvia
2   Max Planck Institute for Solid State Research, Heisenbergstraße 1, D70569 Stuttgart, Germany
*   Correspondence: yuri.mastrikov@cfi.lu.lv

Abstract: Sr-doped lanthanum scandate $La_{1-x}Sr_xScO_{3-\delta}$ (LSS) is a promising perovskite-type material for electrochemical applications such as proton conductors. Oxygen vacancy is a common defect in ABO_3-type perovskites. It controls ion transport as well as proton uptake. The energetic, structural, and electronic properties of oxygen vacancy in LSS are studied deploying the DFT method with meta-GGA functional. The vacancy formation energies in LSS were calculated for various Sr concentrations. Unlike other perovskites, in this material, the electrons are trapped at the oxygen vacancy site (the F-type centres, common in ionic oxides like MgO and Al_2O_3) rather than localised on the nearest to the vacancy B-cations. The process of oxygen vacancy formation is considered relative to Sr concentration x and oxygen nonstoichiometry factor δ. Three primary regimes are discussed: (I) localized at the vacancy electrons, $x/\delta < 2$, (II) electron charge balanced system, $x/\delta = 2$, and (III) delocalized electron holes, $x/\delta > 2$. For $x/\delta \geq 2$ oxygen vacancy formation energy reaches the saturation level of ~3.5 eV, which is potentially beneficial for the proton uptake.

Keywords: lanthanum scandate; oxygen vacancy; oxygen stoichiometry; F-centre; DFT

1. Introduction

Independently discovered in 1998 by Fujii et al. [1] and in 1999 by Lybye et al. [2], proton conductivity in lanthanum scandates made these materials a promising choice for Protonic-Ceramic Fuel Cells (PCFC) and Protonic Ceramic Electrolysis Cell (PCEC). As reported in ref. Nomura, K. et al. [3], Sr-doped lanthanum scandate-$La_{1-x}S_xrScO_{3-\delta}$ showed the highest proton conductivity of ca. 6×10^{-3} S cm^{-1} at 873 K for $x = 0.2$. The high proton conductivity was attributed to the increased number of mobile protons due to the high concentration of oxygen vacancy at $x = 0.2$. Extensive studies on crystal structure, electrical conductivity, water incorporation, oxygen and hydrogen diffusivities of lanthanum-strontium scandate were performed [4–6]. Unlike acceptor-doped $Ba(Zr,Ce)O_3$ materials, $La_{1-x}Sr_xScO_{3-\delta}$ (LSS) oxides demonstrate high stability and protonic conductivity not only in water-containing, but also in reduced and carbon-containing atmospheres [7,8]. This makes lanthanum scandates attractive and prospective not only for PCFC and PCEC applications but also for the electrochemical protonic ceramic membrane reactors for dimerization of methane and production of aromatics from methane, as well as fabrication of hydrogen electrochemical filters for gaseous hydrogen of high purity production and electrochemical separators for hydrogen isotopes.

The proton uptake requires the presence of oxygen vacancies in a host material while an oxygen atom of water molecule heals the vacancy, releasing two protons. The experimental study [9] suggests that oxygen deficiency in $La_{1-x}Sr_xScO_{3-\delta}$ is provided by extended defects and formation of oxygen vacancy is rather unfavourable.

The study [10] of Sr doping in the ABO_3 perovskites have demonstrated a considerable decrease of the vacancy formation enthalpy and thus an increase of vacancy concentration.

Acceptor doping into the $LaScO_3$ oxide causes oxygen deficiency, and recent studies indicate the presence of complex extended defects in the structure, as well as F-centres [11] of different types in reducing atmospheres [12]. The papers [9,13] discuss the possibility of the existence of even a double vacancy in related $SrTiO_3$ and $LaScO_3$ oxides. Recent Nuclear Magnetic Resonance (NMR) studies of the local symmetry in scandates [14,15] show that, contrary to $A^{II}B^{IV}$-type perovskites, e.g., $BaZr_{1-x}Sc_xO_{3-x/2}$, in $LaScO_3$ oxygen stoichiometry relates to the surrounding of Sc cation. Particularly, in single *B*-cation perovskite-type compounds, Sc is solely six-fold coordinated. It implies the existence of various types of boundaries capable of segregating defects, including the oxygen sublattice defects, and the presence of electronic compensation mechanisms, potentially introduced by *3d*-metals.

Being a common defect in perovkite-type materials, oxygen vacancy in lanthanum scandates needs to be considered as one of possible oxygen deficiency mechanisms. In this computational study, we investigate oxygen vacancy formation in undoped as well as Sr-doped lanthanum scandate.

2. Methods

For computational modelling of oxygen vacancy in lanthanum scandate we deployed the computer code VASP 6.1.2 The primary calculation details and the core potential details are given in Tables 1 and 2, respectively. The ideal structure of undoped $LaScO_3$ was completely optimized (Table 3, Table A1, Figure A1). For Sr-doped material and vacancy calculations, the lattice constants were kept fixed. Experimental measurements [16] suggest that lattice constants for doped material (x ≤ 0.09) are only 0.02 Å larger, which is negligible for oxygen vacancy calculations. Although the electronic structure of the ideal compound suggests diamagnetic state, particularly for defect calculations spin-polarization was enabled.

Table 1. Main calculation parameters.

Computer Code.	VASP 6.1.2 [17]
Plane wave basis set cutoff energy	650 eV
Supercell extensions	$\begin{pmatrix} 2 & 0 & 0 \\ 1 & 1 & 1 \\ 1 & 1 & -1 \end{pmatrix}$
K-points	Monkhorst-Pack [18] $2 \times 2 \times 2$
Exchange-correlation functional	Strongly Constrained and Appropriately Normed Semilocal Density Functional (SCAN) [19]
External pressure	<1 kbar
Forces on atoms	<0.02 eV/Å

Table 2. Projector Augmented Wave (PAW) [20] Perdew-Burke-Ernzerhof (PBE) [21] potentials for core electrons.

Potentials	Valence Electrons	E_{cutoff}, eV
La	$5s^25p^66s^25d^1$	219.292
Sr	$4s^24p^65s^2$	229.353
Sc	$3d^14s^2$	154.763
O	$2s^22p^4$	400.000

It is known that the strongest structural perturbation caused by oxygen vacancy in perovskites occurs along the *B-V*o-*B* chain [22]. In case of multiple oxygen vacancies, it is practical to build a supercell with the largest distances along all three mutually orthogonal *B-V*o-*B* chain directions. The extensions [23] of our supercell (Figure A2) provide the smallest volume in a combination with the largest distance along the direction of the strongest interaction between the periodically translated images of oxygen vacancy.

Table 3. Experimentally measured and calculated LaScO$_3$ lattice constants in Å. Atomic coordinates are given in Table A1.

Scheme 0	a_0	b_0	c_0
Clark, J. B. et al. [24]	5.7911	8.0923	5.6748
Farlenkov, A. S. et al. [16]	5.7913	8.0943	5.6793
present study	5.7841	8.0826	5.6680

Although the extensions of the supercell are large enough to limit the Brillouin zone sampling by a single *K*-point, we add one more point in each direction in order to facilitate the convergence.

SCAN exchange-correlation functional was chosen as a feasible alternative to computationally demanding hybrid functionals.

3. Main Results and Discussion

LaScO$_3$ is a perovskite-type single-phase material (Figure A1) with strongly pronounced orthorhombic distortion (*Pnma* space group).

Sr doping was modelled as *A*-cation substitution-Sr$_{La}$. Sr cations were placed as the 4th, the 5th and the 12th nearest neighbours (Table A2). This substitution is compensated by the electron holes delocalized over the oxygen sub-lattice, which determines the oxygen vacancies behaviour and defect formation energetics. There is a negligible, 0.01 and 0.04 eV per Sr$_{La}$, repulsive interaction between Sr$_{La}$ atoms for $x = 0.125$ (Table A3) and 0.25 (Table A4) concentrations, respectively, calculated relative to $x = 0.0625$ Sr-concentration. Such small interaction energy values suggest a homogeneous distribution of the dopant on the host lattice. Oxygen vacancy was introduced as a neutral defect-by removing the neutral atom from the neutral system. Note that in all cases in this study, despite the presence of charged defects, the whole system is kept electroneutral.

A detailed description of oxygen vacancy and Sr$_{La}$ spatial distribution is given in interatomic distances (Appendix A). There are two nonequivalent oxygen atoms in undoped structure-apical and equatorial (Table A1). There are twelve nearest to *A*-cation oxygen anions in perovskite-type structure. Due to the orthorhombic distortion, in LSS we deal with eight coordination subspheres-four for each apical anion and four for each pair of equatorial oxygen anions (Table A2). In doped material, oxygen vacancy was created at all eight inequivalent nearest to Sr cation distances. Formation energy was calculated relative to oxygen molecule (Ref. [10]). Due to the strong dependence on the computational method, the experimental value of O$_2$ binding energy 5.12 eV [25] was used.

To satisfy the formal charge neutrality condition, the value of oxygen nonstoichiometry δ has to be twice smaller than the concentration of Sr dopant x-La$_{1-x}$Sr$_x$ScO$_{3-x/2}$. In many perovskite-type materials, e.g., *A*(Fe,Co)O$_{3-\delta}$, oxygen stoichiometry is stabilized by the adjustment of the oxidation state of *B*-cation [26,27]. Some perovskite-type compounds may provide conditions for both accepting electrons to the *d*-orbitals of *B*-cations as well as trapping them at the vacancy site [10,28–30]. Sc cation, in its turn, demonstrates a strong resistance to accept additional electrons, remaining in the oxidation state 3+. *A*-cations La and Sr do not change their charge easily either. This leads to the formation of the F-type centres [11] in La$_{1-x}$Sr$_x$ScO$_{3-\delta}$. Considering a relatively large band gap of LSS, localization of the electrons of the missing O at the vacancy site is energetically more favourable than on *d*-orbitals of the nearest to the vacancy Sc cations.

It is well known that Sr^{2+} ion substituting for La^{3+} is compensated by electron holes on oxygen *p*-orbitals or oxygen vacancy $V_O^{\bullet\bullet}$ (Kröger-Vink notation [31]). Doping by Sr, as well as $V_O^{\bullet\bullet}$ formation alone, changes the electroneutrality of the system, which has to be compensated. Such $V_O^{\bullet\bullet}$ formation can be described as following

$$2\text{SrO} \rightarrow 2\text{Sr}'_{La} + V_O^{\bullet\bullet} + 2\text{O}_O^x.$$
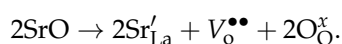
In parallel with the Kröger-Vink notation, we apply commonly accepted in optical physics F-type centre nomenclature. This way we would like to emphasize the material's specific properties of oxygen vacancy. It is also a convenient approach to describe various vacancy formation regimes.

Oxygen vacancies are likely to prevail at high temperatures. In accordance with the present calculations in the electron charge neutral supercells:

(1)　two electrons, due to the $V_o^{\bullet\bullet}$ formation, reside at the vacancy site (the colour F^0-centre [32]) if Sr is absent;

(2)　the substitution Sr'_{La} introduces an electron hole on oxygen p-orbitals;

(3)　Depending on the oxygen vacancy and Sr concentrations, electrons and holes are partially or completely compensated, giving rise to various combinations of F-type centres and electron holes. There are two, one and no electrons, trapped at the vacancy site in F^0-, F^+- and F^{++}-centre, respectively.

Therefore, the following cases were considered (Table 4, Figure 1):

(1)　formation of F^0-centres for $x/\delta = 0$;

(2)　simultaneous formation of both F^0- and F^+- centres for $0 < x/\delta < 1$;

(3)　formation of F^+-centres for $x/\delta = 1$;

(4)　simultaneous formation of both F^+- and F^{++}- centres for $1 < x/\delta < 2$

(5)　formation of F^{++}-centres for $x/\delta = 2$; all electron holes are compensated by the electrons left from the $V_o^{\bullet\bullet}$ for $x/\delta = 2$

(6)　simultaneous formation of both F^{++}-centres and electron holes for $x/\delta > 2$.

Table 4. Share of F-type centres and electron holes in $La_{1-x}Sr_xScO_{3-\delta}$ (Figure 1).

x/δ Range	Defect	Defect Share	Defect	Defect Share
$0 \leq x/\delta \leq 1$	F^0-centre	$1-x/\delta$	F^+-centre	x/δ
$1 \leq x/\delta \leq 2$	F^+-centre	$2-x/\delta$	F^{++}-centre	$x/\delta-1$
$2 \leq x/\delta$	F^{++}-centre	$1/(x/\delta-1)$	electron hole	$(x/\delta-2)/(x/\delta-1)$

Two concentrations of oxygen vacancies were tested in a combination with three concentrations of Sr (Table 5). One ($x = 0.0625$) and two ($x = 0.125$) oxygen vacancies were introduced at various distances from Sr'_{La} cations (Table A2), to estimate the deviation of the formation energy due to the Sr'_{La}-$V_o^{\bullet\bullet}$ interaction. In undoped material vacancy formation energies are extremely high, reaching 8 eV. That makes the defect formation under the normal conditions extremely unfavourable. Even the low concentration of Sr ($x = 6.25\%$) causes an immediate drop in formation energy down to 6.8–6.9 eV per vacancy. Note that vacancy formation energy does not depend solely on Sr concentration x or oxygen stoichiometry δ, but on the particular combination of defects (Table 4), governed by the x/δ ratio. In general, equilibrium oxygen vacancy concentration also strongly depends on oxygen partial pressure, temperature, as well as other factors [33] not considered in our model. The formation energies are still high for $x/\delta < 2$. $x/\delta = 2$ ratio provides the condition for moderate 3.5–3.8 eV oxygen vacancy formation energies while for $x/\delta > 2$ the saturation is clearly reached (Figure 2). Similar saturation effect at $x/\delta > 2$ was also observed by Mizusaki et al. [34] for $La_{1-x}Sr_xFeO_{3-\delta}$. However, there is a great difference between the materials. In $La_{1-x}Sr_xFeO_{3-\delta}$ the electron holes localise on Fe cations, which facilitates the formation of oxygen vacancy with the energy of ~1 eV [29,34].

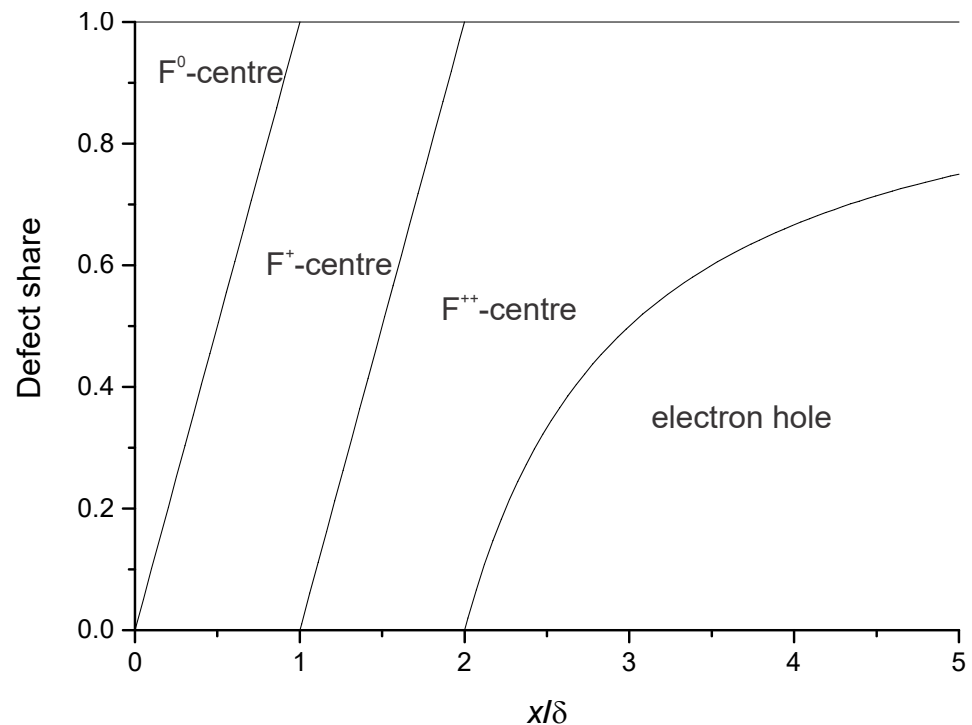**Figure 1.** Share of F-type centres and electron holes in $La_{1-x}Sr_xScO_{3-\delta}$ (Graphical representation of Table 4).

Table 5. Oxygen vacancy (*apical* or *equatorial*, Table A1) formation energy in $La_{1-x}Sr_xScO_{3-\delta}$, in eV per one vacancy. Corresponding spatial distribution of Sr cations as in Tables A3 and A4 and $V_o^{\bullet\bullet}$ as in Tables A5–A8. For $\delta = 0.0625$ a single vacancy was introduced as in Tables A5, A6 and A8. For $\delta = 0.125$, a two vacancies were introduced as in Tables A7 and A9.

		Configuration Matrix	Configuration Number (Table A10)							
			$V_o^{\bullet\bullet}$ *ap.*					$V_o^{\bullet\bullet}$ *eq.*		
x	δ		1	2	3	4	5	6	7	8
0	0.0625		7.89				7.97			
0.0625	0.0625	Table A5	6.77	6.93	6.57	6.55	6.81	6.94	6.97	6.58
0.125	0.0625	Table A6	3.50	3.74	3.87	3.82	3.58	3.74	3.79	3.89
0.125	0.125	Table A7	3.17	3.51	3.53	3.56	3.52	3.45	3.56	3.38
0.25	0.0625	Table A8	6.72	6.88	6.59	6.58	6.77	6.91	6.92	6.59
0.25	0.125	Table A9	3.36	3.76	3.76	3.83	3.75	3.68	3.80	3.78

To our best knowledge, there is no experimentally measured oxygen vacancy formation energy in LSS to compare the calculated values with. However, the authors of Ref. [35] assume that, among other factors, the contribution of the formation energy may be the reason for the the high oxygen diffusion apparent activation energy values for the undoped material. Farlenkov et al. showed that the apparent activation energy for the undoped material (2.7 eV) is much higher than for doped ($x = 0.09, 0.04$) ones (1.2, 1.3 eV).

The electronic properties analysis revealed that calculated band gap of 4.4 eV in comparison to the experimental values of 5.8 eV [36] is underestimated. This underestimate, however, does not affect the main conclusions. The Hubbard correction of *U-J* = 4 eV, expanding the gap by 0.2 eV, was discarded. Oxygen vacancies create distinct defect levels ~ at 0.8, 1.5 and 2.3 eV below the Conduction Band Minimum CBM (Figure 3). A similar peak in DOS was reported by Vlasov et al. in [12] for $x/\delta = 0$ and 2. Our considerations suggest that in both cases there is a single defect level in the band gap, ca. 1.5 eV below the

CBM. The position of the defect levels in that study [12], however, is much closer to the valence band ~0.5 eV, which can be attributed to the computational method applied.
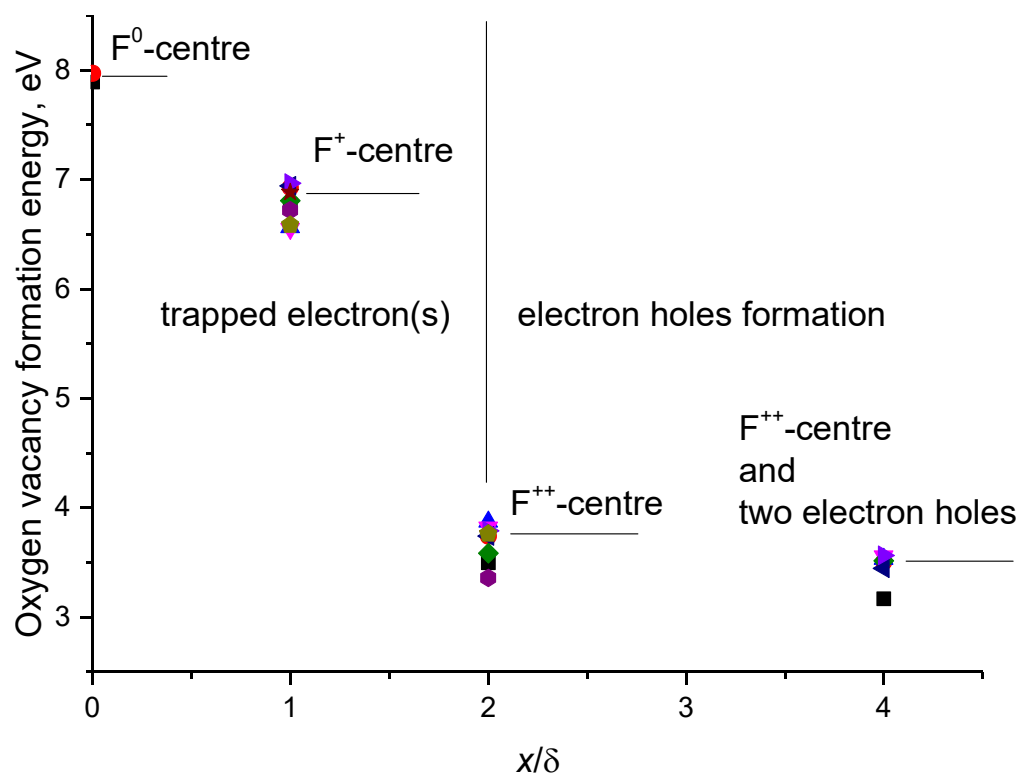

Figure 2. Two regimes of oxygen vacancy formation in $La_{1-x}Sr_xScO_{3-\delta}$ (data from Table 5). Data points of different colours denote different spatial distribution (Tables A5–A9) of Sr'_{La} cations and $V_o^{\bullet\bullet}$ as listed in Table 5.

DOS plots in Figure 3 demonstrate a continuous transition from the $x/\delta = 0$ regime to $x/\delta = 2$ regime via special (Figure 3a,e,i) as well as general (Figure 3b–d,f–h) cases. In the case of $x/\delta = 0$ the single defect level is fully occupied (Figure 3a). The electron density distribution analysis shows that the electrons on this defect level are located right at the vacancy site (Figure 4a) rather than on the *d*-orbitals of the nearest *B*-cations as in Refs. [37–39]. This is also confirmed by a negligible (<0.05 *e*) deviation of electron charges (Bader) on *A*- as well as *B*-cations. So, the charge redistribution caused by oxygen vacancy occurs predominantly between oxygen *p*-orbitals and the vacancy site. There are two defect levels for $x/\delta = 1$-occupied and unoccupied in the spin up and spin down channel, respectively (Figure 3e). A single unpaired electron is trapped at the vacancy site (Figure 4a). For $x/\delta = 1.5$, with the equal numbers of F⁺- and F⁺⁺-centers in the system we observed a split of the central (F⁰-, F⁺⁺-centre) peaks, merging the F⁺-centre peaks (Figure 3g). For $x/\delta = 2$ the vacancy site is unoccupied (Figure 3i) and Valence Band Maximum (VBM) is composed solely by the *p*-orbitals of all oxygen ions (Figure 4b). For $x/\delta = 4$ the vacancy site remains unoccupied. In addition to that, two uncompensated electron holes appear.

The density of states analysis has confirmed that in a general case (Figure 3b–d,f–h) there is a superposition of two types of noninteracting defects, as described in Table 4 and shown in Figure 1. Note that in a combination of two defects (Figure 3b–d,f–h) the size of the defect peaks is proportional to the share of the corresponding defect (Table 4). In special cases ($x/\delta = 0, 1, 2$) we can assume the presence of just one particular type of defects (F⁰-, F⁺- or F⁺⁺-centre) with one Figure 3a,i or two peaks Figure 3e. The positions of these three peaks relative to CBM remain practically the same for all combinations of defects.
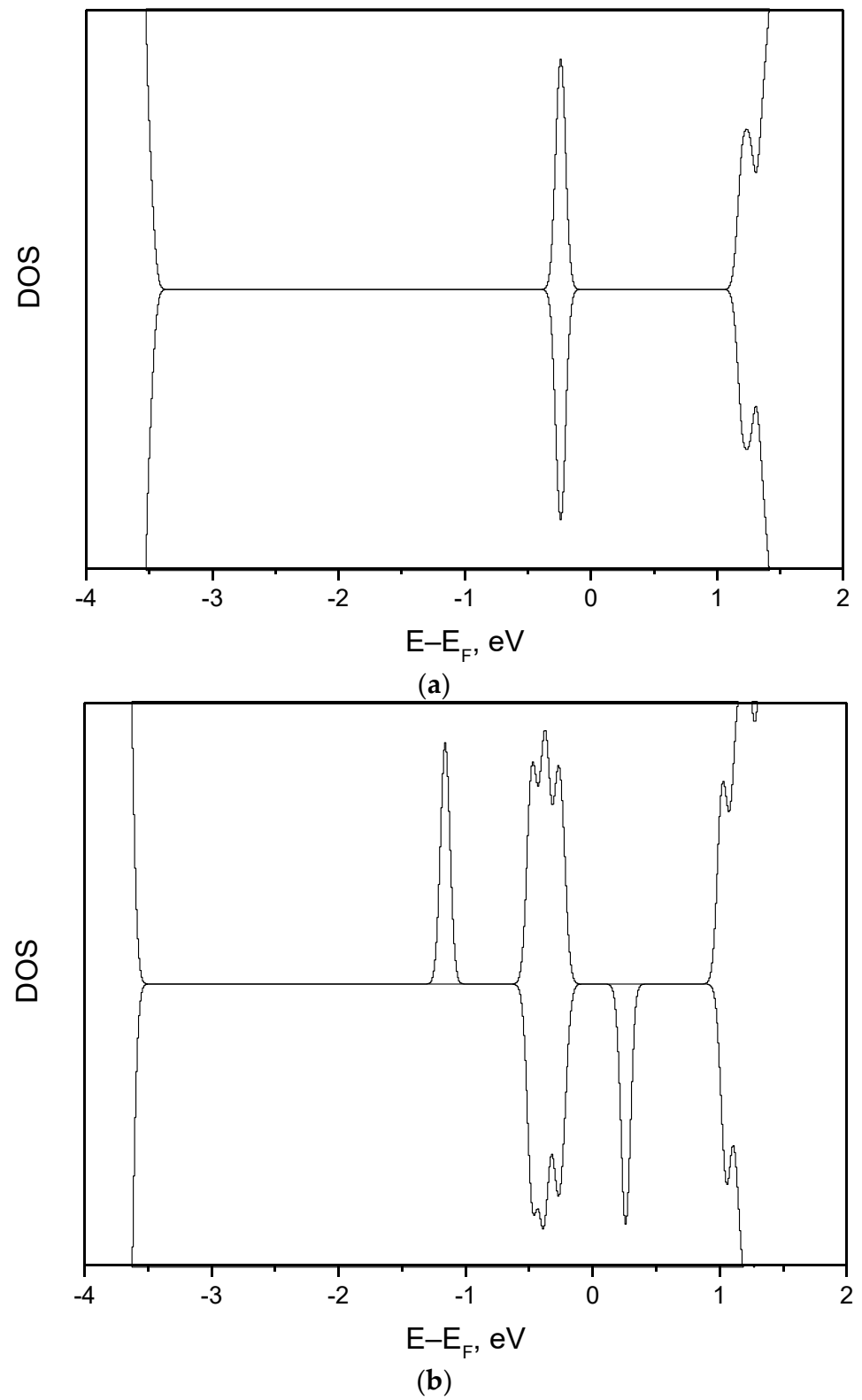
(**a**)

(**b**)
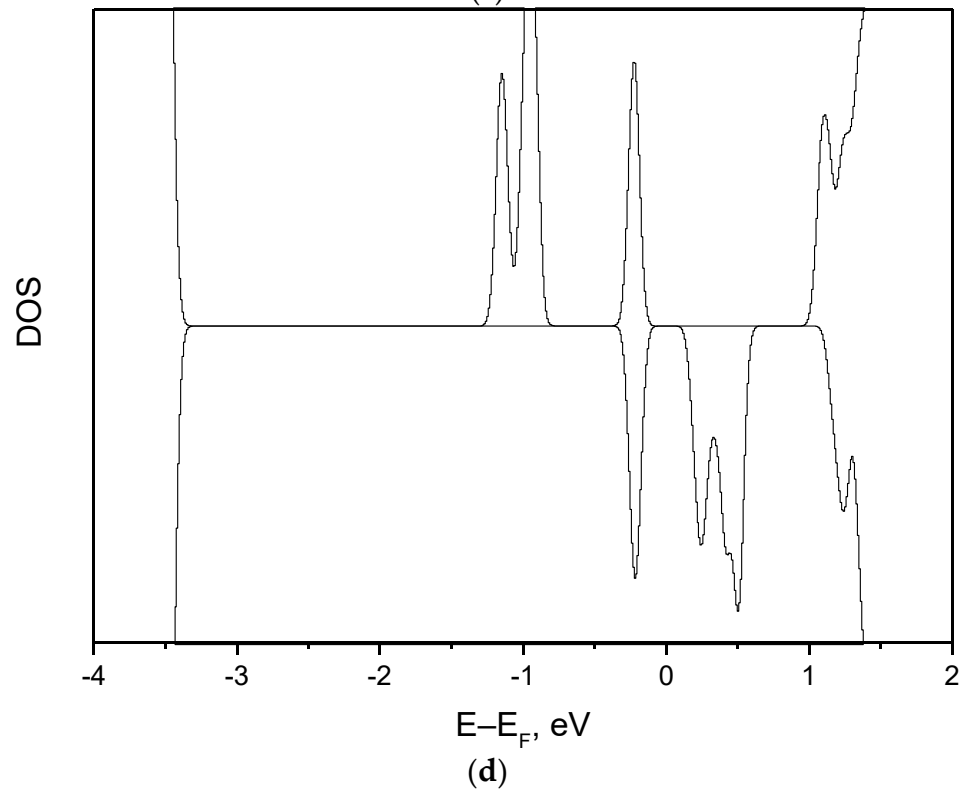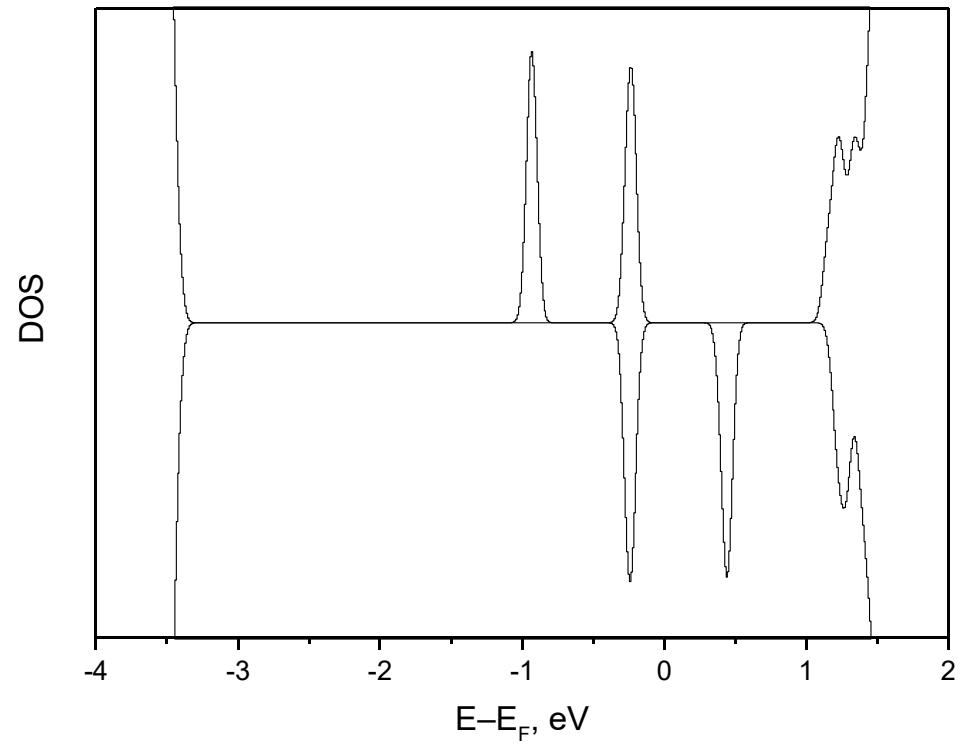
Figure 3. *Cont.*

(**c**)

(**d**)

Figure 3. *Cont.*

(**e**)

(**f**)

Figure 3. *Cont.*
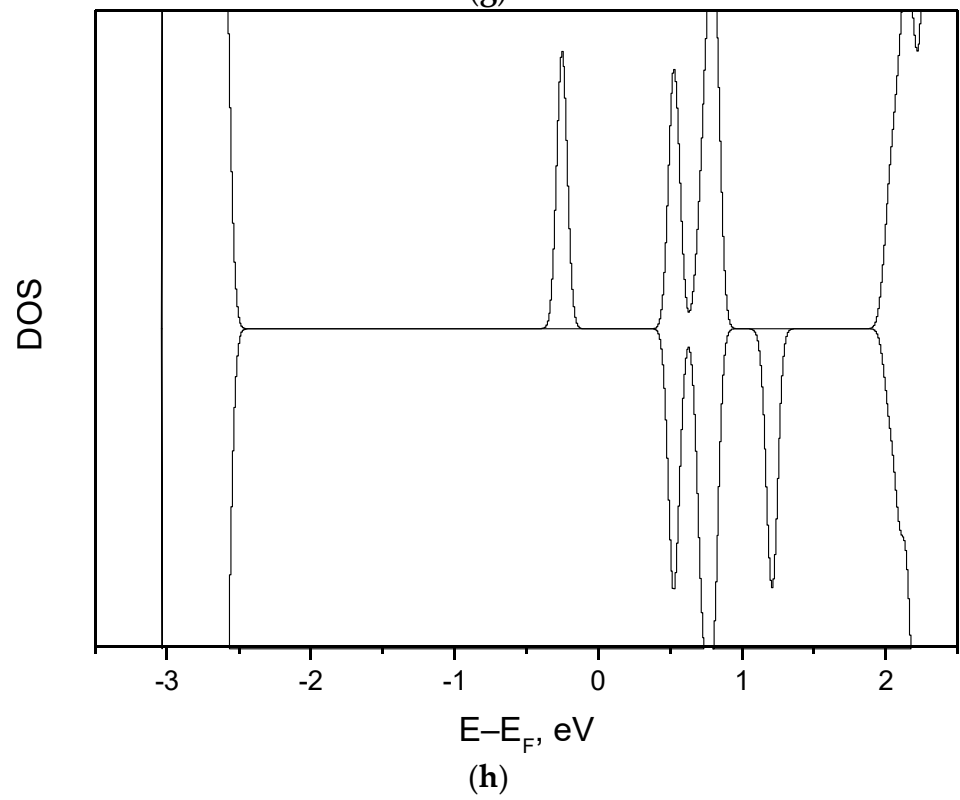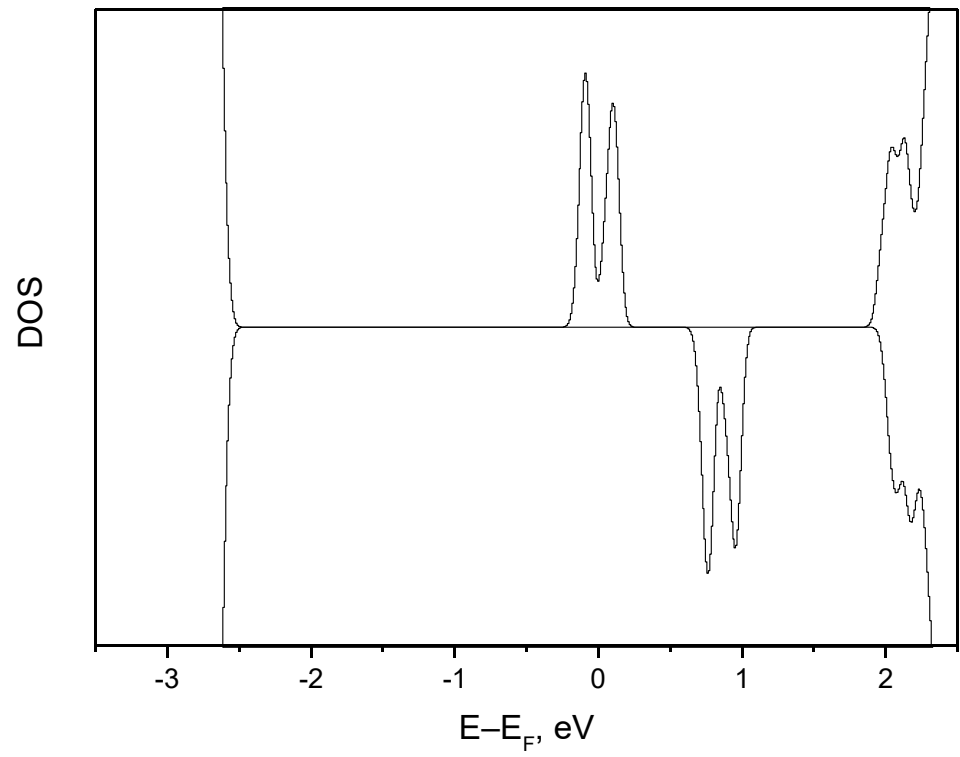
(**g**)

(**h**)

Figure 3. *Cont.*

(i)
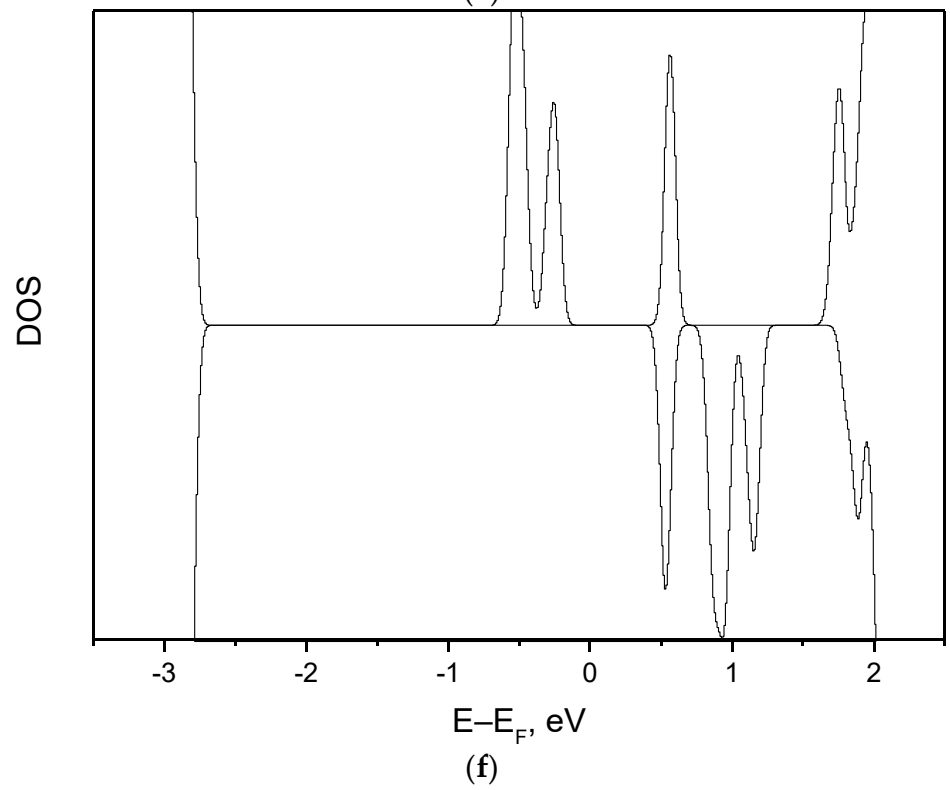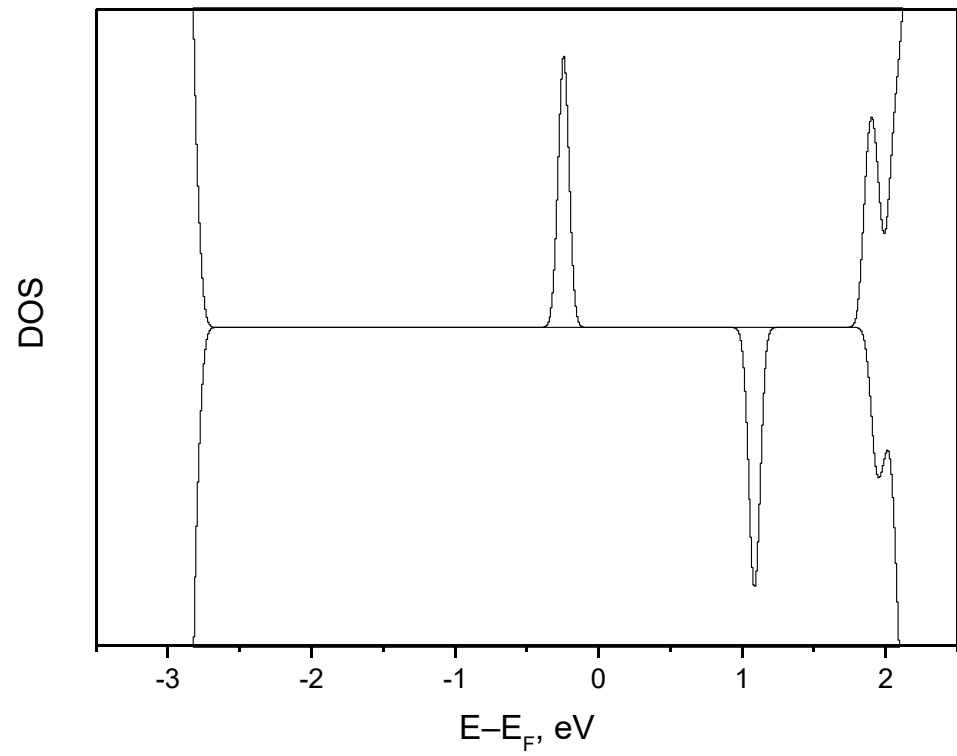
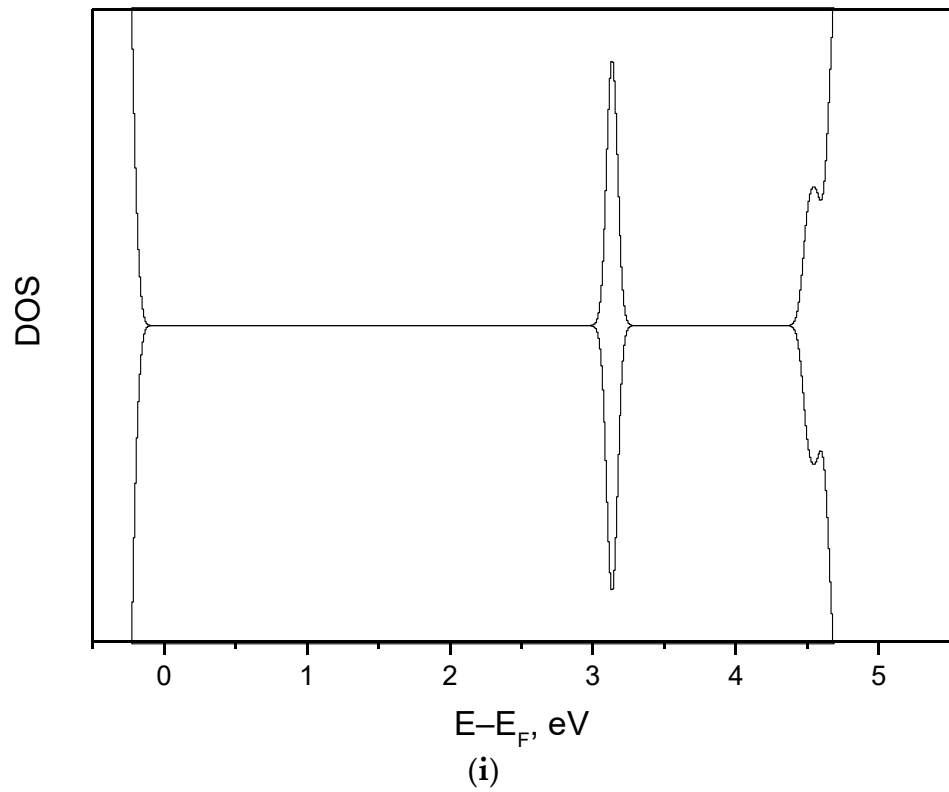**Figure 3.** Density of states (DOS) for various combinations of F-type centres, as described in Table 4 and shown in Figure 1. (**a**) 0. (**b**) 0.25. (**c**) 0.5. (**d**) 0.75. (**e**) 1. (**f**) 1.25. (**g**) 1.5. (**h**) 1.75. (**i**) 2.
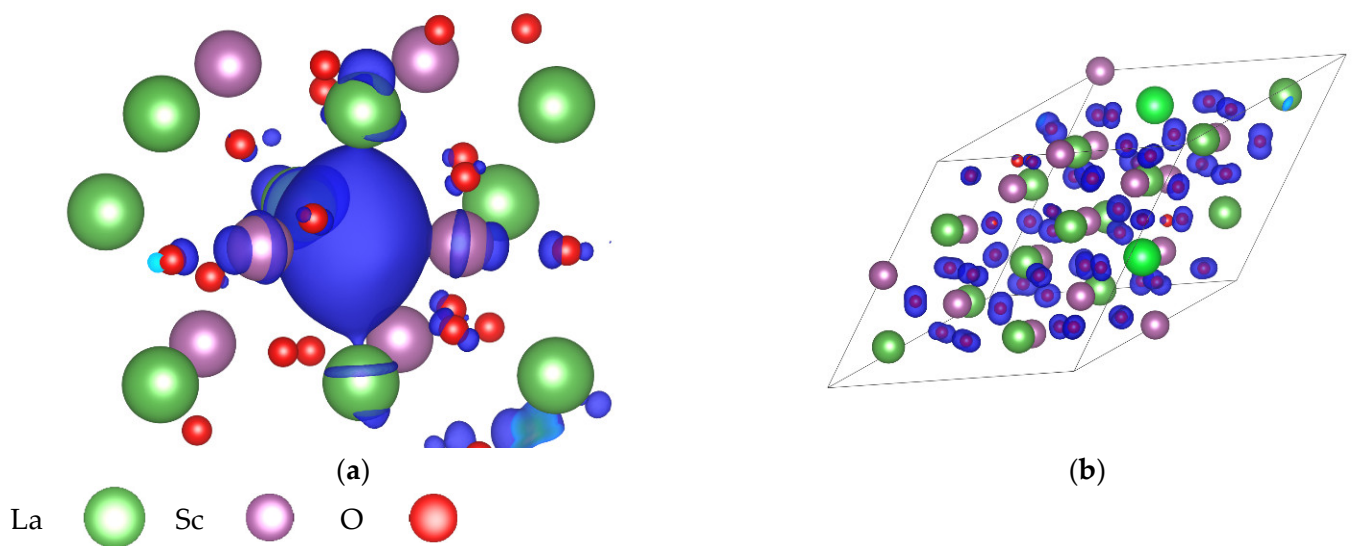

(a)

La   Sc   O

(b)

Figure 4. Orbital-projected electron density of F^0-, F^+- and F^{++}-centres (**a**) and electron holes on oxygen *p*-orbitals (**b**).

Summing this Section up, we have shown that oxygen vacancy formation in $La_{1-x}Sr_xScO_{3-\delta}$ solid solutions is controlled predominantly by the dopant Sr concentration x. Oxygen nonstoichiometry factor δ is very close to $x/2$ or slightly larger, for higher temperatures and lower p_{O_2}. Large diviations from this value energetically are very costly. This makes oxygen vacancy formation in undoped material (F^0-centre) extremely unfavourable (~8 eV). For Sr-doped compounds the vast majority (x/δ-1) of vacancies will be presented as F^{++}-centres (~3.5 eV) with an extremely small (2-x/δ) share of F^+-centres (~7 eV). This correlates with the available experimental data on oxygen diffusion coefficient [35]. For x/δ slightly smaller than 2, electrons, uncompensated by holes, convert F^{++}- into F^+-centres. Detailed studies oxygen vacancy in commonly used perovskite-type materials (A = Sr, Ba, La, Pb; B = Ti, Fe, Co, Zr) revealed that two electrons are predominantly localized on d-orbitals of the nearest to the vacancy B-cations [10,29,30,40]. This is in contrast with LSS perovskites studied here, where electron localization within the vacancy itself (trapping) is similar to that in binary ionic oxides (MgO, Al_2O_3) [41–44]. This effect can be attributed to the Sc electron structure with completely unoccupied $3d$-orbitals in 3+ oxidation state, making the electron transfer from the valence band energetically unfavourable.

Obtained data covers the whole range of x/δ values, predicting formation of the F-type colour centres with optical absorption in infrared (IR) region of 0.8–2.3 eV.

4. Conclusions

Controlled mainly by doping, e.g., Sr substituting for B-cation, oxygen deficiency in ABO_3 type perovskites usually affects the oxidation state of the transition metal B-cations. However, in contrast to other transition metals with open d-orbitals, scandium demonstrates predominantly a single oxidation state-3+, which follows from its electron structure-[Ar] $3d^14s^2$. In $La_{1-x}Sr_xScO_{3-\delta}$ studied here, oxygen stoichiometry is controlled by mixing A^{3+}- with A^{2+}-cations (La with Sr). We have demonstrated, that unlike most of ABO_3 perovskites, electrons are trapped right at the oxygen vacancy site, like in MgO and other ionic oxides, rather than localise on the two nearest B-cations. We also predicted the optical absorption of the neutral vacancies (F^0-centres with two trapped electrons) to be in the IR region. Lastly, we predicted that Sr doping strongly reduces the vacancy energy formation, which facilitates the proton uptake in this material.

Conflicts of Interest: Authors declare no conflict of interests.
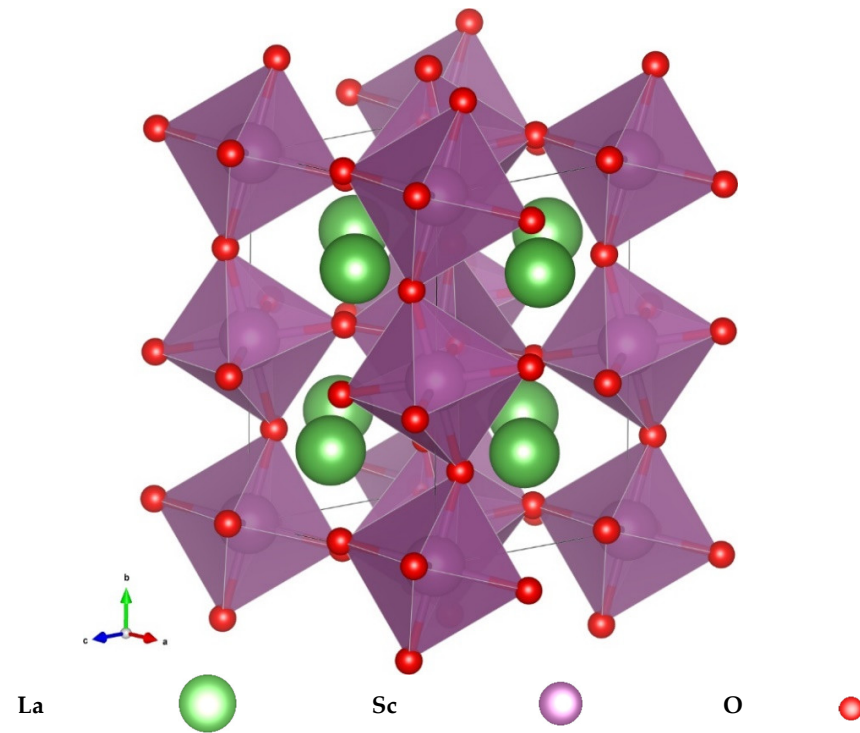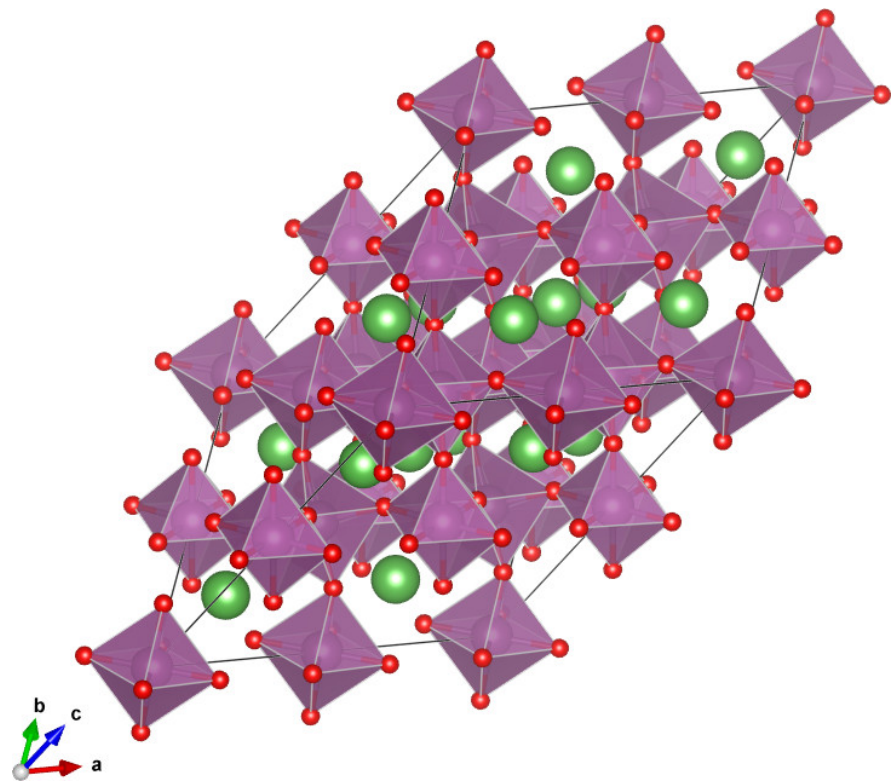
Appendix A

Figure A1. Optimized crystal structure of $LaScO_3$.

Figure A2. $\begin{pmatrix} 2 & 0 & 0 \\ 1 & 1 & 1 \\ 1 & 1 & -1 \end{pmatrix}$-extended supercell. See Figure A1 for atom labels.

The spatial configuration of defects in a host lattice can be uniquely described as a set of each-to-each interdefect distances (Mastrikov-Koch notation [45]). A Radial Distribution Function is calculated for each pair of defects (Table A2). Then, each particular configuration is presented in a form of a matrix with mutual distances between each defect (Tables A3 and A9). For these calculations eight sets of interdefect distances were used (Table A10). These sets are used as submatrices within the primary configuration matrices (Tables A3 and A9).

Table A1. Atomic coordinates of LaScO$_3$.

		Atomic Coordinate					
		x		**y**		**z**	
Atom	Site	a^*	b^*	a^*	b^*	a^*	b^*
La	4c	0.43745	0.45054	0.25	0.25	0.01537	0.01127
Sc	4a	0	0	0	0	0	0
O apical	4c	0.5323	0.53270	0.25	0.25	0.5996	0.59797
O equatorial	8d	0.1988	0.20025	0.0528	0.05160	0.3044	0.30048

$^*a$ -Ref. [24]; $^*b$ -present study.

Table A2. Radial Distribution Function of Sr-Sr, Sr-O$_{apical}$, Sr-O$_{equatorial}$, O$_{apical}$-O$_{apical}$, and O$_{equatorial}$-O$_{equatorial}$ sublattices.

Sr-Sr	Distance, Å
4	5.44
5	5.62
12	8.05
Sr-O$_{ap.}$	
1	2.37
2	2.50
3	3.33
4	3.42
5	4.59
6	4.93
7	5.04
8	5.28
9	5.57
13	5.81
14	6.04
15	6.26
22	7.32
Sr-O$_{eq.}$	
1	2.40
2	2.70
3	2.84
4	3.60
5	4.55
6	4.75
8	4.90
9	5.00
12	5.60
14	5.82
15	5.93
16	6.11
18	6.50
27	7.28
33	7.85
O$_{ap.}$-O$_{ap.}$	
13	8.049
O$_{eq.}$-O$_{eq.}$	
33	8.049

Table A3. Configurational Matrix (mutual interatomic distances in NN, as in Table A2) for x = 0.125.

	Sr1	**Sr2**
Sr1	0	Sr-Sr 12
Sr2		0

Table A4. Configurational Matrix (mutual interatomic distances in NN, as in Table A2) for x = 0.25.

	Sr1	**Sr2**	**Sr3**	**Sr4**
Sr1	0	Sr-Sr 12	Sr-Sr 4	Sr-Sr 4
Sr2		0	Sr-Sr 4	Sr-Sr 4
Sr3			0	Sr-Sr 5
Sr4				0

Table A5. Configurational Matrix (mutual interatomic distances in NN, as in Table A2) for x = 0.0625, δ = 0.0625. Five configurations (A), as in Table A10.

	Sr1	**Vo**
Sr1	0	A
Vo		0

Table A6. Configurational Matrix (mutual interatomic distances in NN, as in Table A2) for x = 0.125, δ = 0.0625. Five configurations (A,B), as in Table A10.

	Vo
Table A3	A
	B
Vo	0

Table A7. Configurational Matrix (mutual interatomic distances in NN, as in Table A2) for x = 0.125, δ = 0.125. Five configurations (A,B,C), as in Table A10.

	Vo1	**Vo2**
Table A3	A	B
	B	A
Vo1	0	C
Vo2		0

Table A8. Configurational Matrix (mutual interatomic distances in NN, as in Table A2) for x = 0.25, δ = 0.0625. Five configurations (A,B,D,E), as in Table A10.

	Vo
Table 4	A
	B
	D
	E
Vo	0

Table A9. Configurational Matrix (mutual interatomic distances in NN, as in Table A2) for x = 0.25, δ = 0.125. Five configurations (A,B,C,D,E,F,G), as in Table A10.

		Vo1	Vo2
		A	B
Table A4		B	A
		D	F
		E	G
Vo1		0	C
Vo2			0

Table A10. Eight configurations -1-5, with the interatomic distances as in Table A2.

	1	2	3	4	5	6	7	8
A	Sr-$O_{ap.}$ 1	Sr-$O_{ap.}$ 2	Sr-$O_{ap.}$ 3	Sr-$O_{ap.}$ 4	Sr-$O_{eq.}$ 1	Sr-$O_{eq.}$ 2	Sr-$O_{eq.}$ 3	Sr-$O_{eq.}$ 4
B	Sr-$O_{ap.}$ 15	Sr-$O_{ap.}$ 14	Sr-$O_{ap.}$ 13	Sr-$O_{ap.}$ 9	Sr-$O_{eq.}$ 18	Sr-$O_{eq.}$ 16	Sr-$O_{eq.}$ 14	Sr-$O_{eq.}$ 15
C	$O_{ap.}$-$O_{ap.}$ 13	$O_{ap.}$-$O_{ap.}$ 13	$O_{ap.}$-$O_{ap.}$ 13	$O_{ap.}$-$O_{ap.}$ 13	O_{eq}-O_{eq} 33	O_{eq}-O_{eq} 33	O_{eq}-O_{eq} 33	O_{eq}-O_{eq} 33
D	Sr-$O_{ap.}$ 6	Sr-$O_{ap.}$ 5	Sr-$O_{ap.}$ 7	Sr-$O_{ap.}$ 22	Sr-$O_{eq.}$ 4	Sr-$O_{eq.}$ 12	Sr-$O_{eq.}$ 16	Sr-$O_{eq.}$ 33
E	Sr-$O_{ap.}$ 7	Sr-$O_{ap.}$ 8	Sr-$O_{ap.}$ 6	Sr-$O_{ap.}$ 5	Sr-$O_{eq.}$ 9	Sr-$O_{eq.}$ 14	Sr-$O_{eq.}$ 8	Sr-$O_{eq.}$ 1
F	Sr-$O_{ap.}$ 6	Sr-$O_{ap.}$ 5	Sr-$O_{ap.}$ 7	Sr-$O_{ap.}$ 8	Sr-$O_{eq.}$ 15	Sr-$O_{eq.}$ 27	Sr-$O_{eq.}$ 2	Sr-$O_{eq.}$ 6
G	Sr-$O_{ap.}$ 7	Sr-$O_{ap.}$ 22	Sr-$O_{ap.}$ 6	Sr-$O_{ap.}$ 5	Sr-$O_{eq.}$ 7	Sr-$O_{eq.}$ 3	Sr-$O_{eq.}$ 5	Sr-$O_{eq.}$ 18

References

1. Fujii, H.; Katayama, Y.; Shimura, T.; Iwahara, H. Protonic Conduction in Perovskite-Type Oxide Ceramics Based on $LnScO_3$ (Ln = La, Nd, Sm or Gd) at High Temperature. *J. Electroceramics* **1998**, *2*, 119–125. [CrossRef]
2. Lybye, D.; Bonanos, N. Proton and Oxide Ion Conductivity of Doped $LaScO_3$. *Solid State Ion.* **1999**, *125*, 339–344. [CrossRef]
3. Nomura, K.; Takeuchi, T.; Kamo, S.; Kageyama, H.; Miyazaki, Y. Proton Conduction in Doped $LaScO_3$ Perovskites. *Solid State Ion.* **2004**, *175*, 553–555. [CrossRef]
4. Stroeva, A.Y.; Gorelov, V.P. Nature of Conductivity of Perovskites $La_{1-X}Sr_XSco_{3-\alpha}$ (X = 0.01-0.15) under Oxidative and Reducing Conditions. *Russ. J. Electrochem.* **2012**, *48*, 1079–1085. [CrossRef]
5. Farlenkov, A.S.; Putilov, L.P.; Ananyev, M.V.; Antonova, E.P.; Eremin, V.A.; Stroeva, A.Y.; Sherstobitova, E.A.; Voronin, V.I.; Berger, I.F.; Tsidilkovski, V.I.; et al. Water Uptake, Ionic and Hole Transport in $La_{0.9}Sr_{0.1}Sco_{3-\alpha}$. *Solid State Ion.* **2017**, *306*, 126–136. [CrossRef]
6. Farlenkov, A.S.; Vlasov, M.I.; Porotnikova, N.M.; Bobrikov, I.A.; Khodimchuk, A.V.; Ananyev, M.V. Hydrogen Diffusivity in the Sr-Doped $LaScO_3$ Proton-Conducting Oxides. *Int. J. Hydrog. Energy* **2020**, *45*, 23455–23468. [CrossRef]
7. Ananyev, M.V.; Farlenkov, A.S.; Kurumchin, E.K. Isotopic Exchange between Hydrogen from the Gas Phase and Proton-Conducting Oxides: Theory and Experiment. *Int. J. Hydrog. Energy* **2018**, *43*, 13373–13382. [CrossRef]
8. Ananyev, M.V.; Zakharov, D.M. H/D Isotopic Exchange between Methane and a Proton-Conducting Oxide: Theory and Experiment. *Catal. Sci. Technol.* **2020**, *10*, 3561–3571. [CrossRef]
9. Ananyev, M.V.; Farlenkov, A.S.; Zhigalina, O.M.; Khmelenin, D.N.; Atanova, A.V.; Basu, V.G. Antiphase Boundary Defects in Strontium Doped Lanthanum Scandate. *Phys. Status Solidi B* **2021**, *259*, 2100376. [CrossRef]
10. Gryaznov, D.; Baumann, S.; Kotomin, E.A.; Merkle, R. Comparison of Permeation Measurements and Hybrid Density-Functional Calculations on Oxygen Vacancy Transport in Complex Perovskite Oxides. *J. Phys. Chem. C* **2014**, *118*, 29542–29553. [CrossRef]
11. Schulman, J.H. *Color Centers in Solids/by James H. Schulman and W. Dale Compton.*; International series of monographs on solid state physics ; Macmillan: New York, NY, USA, 1962.
12. Vlasov, M.I.; Zainullina, V.M.; Korotin, M.A.; Farlenkov, A.S.; Ananyev, M.V. Effect of Proton Uptake on the Structure of Energy Levels in the Band-Gap of Sr-Doped $LaScO_3$: Diffuse Reflectance Spectroscopy and Coherent Potential Approximation Calculations. *Phys. Chem. Chem. Phys.* **2019**, *21*, 7989–7995. [CrossRef]
13. Lechermann, F.; Jeschke, H.O.; Kim, A.J.; Backes, S.; Valenti, R. Electron Dichotomy on the SrTiO3 Defect Surface Augmented by Many-Body Effects. *Phys. Rev. B* **2016**, *93*, 121103. [CrossRef]
14. Johnston, K.E.; Mitchell, M.R.; Frédé, F.; Blanc, F.; Lightfoot, P.; Ashbrook, S.E. Structural Study of $La_{1-x}Y_xSco_3$, Combining Neutron Diffraction, Solid-State NMR, and First-Principles DFT Calculations. *J. Phys. Chem. C* **2013**, *117*, 2252–2265. [CrossRef]
15. Oikawa, I.; Ando, M.; Kiyono, H.; Tansho, M.; Shimizu, T.; Maekawa, H. On the Symmetry of Defects in Perovskite-Type Protonic Conductors:A Sc-45 NMR Study. *Solid State Ion.* **2012**, *213*, 14–17. [CrossRef]
16. Farlenkov, A.S.; Smolnikov, A.G.; Ananyev, M.V.; Khodimchuk, A.V.; Buzlukov, A.L.; Kuzmin, A.V.; Porotnikova, N.M. Local Disorder and Water Uptake in $La_{1-X}Sr_xScO_{3-\delta}$. *Solid State Ion.* **2017**, *306*, 82–88. [CrossRef]

17. Kresse, G.; Furthmüller, J. Efficient Iterative Schemes for Ab Initio Total-Energy Calculations Using a Plane-Wave Basis Set. *Phys. Rev. B* **1996**, *54*, 11169–11186. [CrossRef]

18. Monkhorst, H.J.; Pack, J.D. Special Points for Brillouin-Zone Integrations. *Phys. Rev. B* **1976**, *13*, 5188–5192. [CrossRef]

19. Sun, J.; Ruzsinszky, A.; Perdew, J.P. Strongly Constrained and Appropriately Normed Semilocal Density Functional. *Phys. Rev. Lett.* **2015**, *115*, 036402. [CrossRef]

20. Blöchl, P.E. Projector Augmented-Wave Method. *Phys. Rev. B* **1994**, *50*, 17953–17979. [CrossRef]

21. Perdew, J.P.; Burke, K.; Ernzerhof, M. Generalized Gradient Approximation Made Simple. *Phys. Rev. Lett.* **1996**, *77*, 3865–3868. [CrossRef]

22. Carrasco, J.; Illas, F.; Lopez, N.; Kotomin, E.A.; Zhukovskii, Y.F.; Evarestov, R.A.; Mastrikov, Y.A.; Piskunov, S.; Maier, J. First-Principles Calculations of the Atomic and Electronic Structure of F Centers in the Bulk and on the (001) Surface of SrTi O_3. *Phys. Rev. B Condens. Matter Mater. Phys.* **2006**, *73*, 064106. [CrossRef]

23. Arnold, H. Transformations of the Coordinate System (Unit-Cell Transformations). In *International Tables for Crystallography*; John Wiley & Sons, Ltd.: Hoboken, NJ, USA, 2006; pp. 78–85. [CrossRef]

24. Clark, J.B.; Richter, P.W.; Toit, L.D. High-Pressure Synthesis of $YScO_3$, $HoScO_3$, $ErScO_3$, and $TmScO_3$, and a Reevaluation of the Lattice Constants of the Rare Earth Scandates. *J. Solid State Chem.* **1978**, *23*, 129–134. [CrossRef]

25. Huber, K.P.; Herzberg, G. Constants of Diatomic Molecules. In *Molecular Spectra and Molecular Structure: IV. Constants of Diatomic Molecules*; Springer: Boston, MA, USA, 1979; pp. 8–689. [CrossRef]

26. Jia, T.; Zeng, Z.; Zhang, X.; Ohodnicki, P.; Chorpening, B.; Hackett, G.; Lekse, J.; Duan, Y. The Influence of Oxygen Vacancy on the Electronic and Optical Properties of $ABO_{3-\delta}$ (A = La, Sr, B = Fe, Co) Perovskites. *Phys. Chem. Chem. Phys.* **2019**, *21*, 20454–20462. [CrossRef]

27. Kotiuga, M.; Zhang, Z.; Li, J.; Rodolakis, F.; Zhou, H.; Sutarto, R.; He, F.; Wang, Q.; Sun, Y.; Wang, Y.; et al. Carrier Localization in Perovskite Nickelates from Oxygen Vacancies. *Proc. Natl. Acad. Sci. USA* **2019**, *116*, 21992–21997. [CrossRef]

28. Janotti, A.; Varley, J.B.; Choi, M.; de Walle, C.G. Vacancies and Small Polarons in $SrTiO_3$. *Phys. Rev. B* **2014**, *90*, 85202. [CrossRef]

29. Gryaznov, D.; Merkle, R.; Kotomin, E.A.; Maier, J. Ab Initio Modelling of Oxygen Vacancies and Protonic Defects in $La_{1-X}Sr_xFeO_{3-\delta}$ Perovskite Solid Solutions. *J. Mater. Chem. A* **2016**, *4*, 13093–13104. [CrossRef]

30. Gryaznov, D.; Blokhin, E.; Sorokine, A.; Kotomin, E.A.; Evarestov, R.A.; Bussmann-Holder, A.; Maier, J. A Comparative Ab Initio Thermodynamic Study of Oxygen Vacancies in ZnO and $SrTiO_3$: Emphasis on Phonon Contribution. *J. Phys. Chem. C* **2013**, *117*, 13776–13784. [CrossRef]

31. Kröger, F.A.; Vink, H.J. Relations between the Concentrations of Imperfections in Crystalline Solids. In *Solid State Physics*; Seitz, F., Turnbull, D., Eds.; Academic Press: Cambridge, MA, USA, 1956; Volume 3, pp. 307–435. [CrossRef]

32. Popov, A.I.; Kotomin, E.A.; Maier, J. Basic Properties of the F-Type Centers in Halides, Oxides and Perovskites. *Nucl. Instrum. Methods Phys. Res. Sect. B Beam Interact. Mater. At.* **2010**, *268*, 3084–3089. [CrossRef]

33. Wexler, R.B.; Gautam, G.S.; Stechel, E.B.; Carter, E.A. Factors Governing Oxygen Vacancy Formation in Oxide Perovskites. *J. Am. Chem. Soc.* **2021**, *143*, 13212–13227. [CrossRef]

34. Mizusaki, J.; Yoshihiro, M.; Yamauchi, S.; Fueki, K. Thermodynamic Quantities and Defect Equilibrium in the Perovskite-Type Oxide Solid Solution $La_{1-x}Sr_xFeO_{3-\delta}$. *J. Solid State Chem.* **1987**, *67*, 1–8. [CrossRef]

35. Farlenkov, A.S.; Khodimchuk, A.V.; Shevyrev, N.A.; Stroeva, A.Y.; Fetisov, A.V.; Ananyev, M.V. Oxygen Isotope Exchange in Proton-Conducting Oxides Based on Lanthanum Scandates. *Int. J. Hydrog. Energy* **2019**, *44*, 26577–26588. [CrossRef]

36. Liu, J.; Iguchi, F.; Sata, N.; Yugami, H. Optical Absorption of Sr-Doped $LaScO_3$ Single Crystals. *Solid State Ion.* **2007**, *178*, 521–526. [CrossRef]

37. Al-Zubi, A.; Bihlmayer, G.; Blügel, S. Electronic Structure of Oxygen-Deficient $SrTiO_3$ and Sr_2TiO_4. *Crystals* **2019**, *9*, 580. [CrossRef]

38. Alexandrov, V.E.; Kotomin, E.A.; Maier, J.; Evarestov, R.A. First-Principles Study of Bulk and Surface Oxygen Vacancies in $SrTiO_3$ Crystal. *Eur. Phys. J. B* **2009**, *72*, 53–57. [CrossRef]

39. Ricci, D.; Bano, G.; Pacchioni, G.; Illas, F. Electronic Structure of a Neutral Oxygen Vacancy in $SrTiO_3$. *Phys. Rev. B* **2003**, *68*, 224105. [CrossRef]

40. Kotomin, E.A.; Zhukovskii, Y.F.; Piskunov, S.; Ellis, D.E. Hybrid DFT Calculations of the F Centers in Cubic $ABO3$ Perovskites. *J. Phys. Conf. Ser.* **2008**, *117*, 12019. [CrossRef]

41. Shluger, A.L.; Stoneham, A.M. Small Polarons in Real Crystals: Concepts and Problems. *J. Phys. Condens. Matter* **1993**, *5*, 3049–3086. [CrossRef]

42. Sharma, R.R.; Stoneham, A.M. Theory of the F Surface Centre in MgO. *J. Chem. Soc. Faraday Trans. 2* **1976**, *72*, 913–919. [CrossRef]

43. Dicks, O.A.; Shluger, A.L. Theoretical Modeling of Charge Trapping in Crystalline and Amorphous Al_2O_3. *J. Phys. Condens. Matter* **2017**, *29*, 314005. [CrossRef]

44. Devreese, J.T.; Fomin, V.M.; Pokatilov, E.P.; Kotomin, E.A.; Eglitis, R.; Zhukovskii, Y.F. Theory of Bound Polarons in Oxide Compounds. *Phys. Rev. B* **2001**, *63*, 184304. [CrossRef]

45. Mastrikov, Y.A.; Sokolov, M.N.; Koch, S.; Zhukovskii, Y.F.; Gopejenko, A.; Vladimirov, P.V.; Borodin, V.A.; Kotomin, E.A.; Möslang, A. Ab Initio Modelling of the Initial Stages of the ODS Particle Formation Process. *Nucl. Instrum. Methods Phys. Res. Sect. B Beam Interact. Mater. At.* **2018**, *435*, 70–73. [CrossRef]